atmosphere

Article

Study on Data Quality Control Method for X-Band Precipitation Radar in Complex Mountainous Areas

Xiaoning Li [1], Xiaowan Liu [2,3], Bin Zou [2], Yan Wang [1], Zewen Guan [4] and Min Xie [2,3,*]

1 Information Center of the Gansu Provincial Department of Water Resources, Lanzhou 730000, China
2 China Institute of Water Resources and Hydropower Research, Beijing 100038, China
3 Ministry of Water Resources Flood Control, Drought Relief, and Disaster Reduction Technology Innovation Center, Beijing 100038, China
4 College of Information Engineering, Inner Mongolia University of Technology, Hohhot 010051, China
* Correspondence: xiemin@iwhr.com

Abstract

X-band rainfall radar systems offer advantages such as high spatial resolution, flexible deployment options, and strong near-surface detection capabilities. However, due to the short electromagnetic wavelength in this band, the radar base data are highly susceptible to multiple coupled factors—including clutter from mountain vegetation, tall buildings, and other terrain features; electromagnetic interference from surrounding radio-frequency equipment; beam obstruction caused by complex topography; and attenuation of rainfall intensity along the precipitation path—resulting in pronounced distortion of raw echoes. This distortion significantly hinders the accuracy of quantitative precipitation estimation in mountainous regions and makes it difficult to meet the operational requirements for precise mountain torrent early warning systems. To address the problem, this study utilizes real-time observational data from field deployments of X-band rainfall radars in mountainous regions to construct a comprehensive, progressive quality control system comprising: refined removal of terrain clutter; electromagnetic interference pre-suppression; dynamic beam obstruction correction; and adaptive rainfall intensity attenuation correction. The terrain clutter suppression algorithm is optimized in this study, and an adaptive beam-blockage compensation algorithm based on the terrain-blockage fraction is further adopted. However, beam-blockage correction exhibits limited improvement in this case, which is likely attributed to the complementary observational coverage provided by higher-elevation radar scans. The echo-missing regions are dynamically corrected according to the terrain-blockage coverage ratio at different elevation angles and azimuths to realize differentiated compensation corresponding to blockage severity so as to effectively restore the true echo intensity obscured by terrain. Furthermore, considering the prominent rain-induced attenuation of radar electromagnetic waves along the propagation path, a dynamic attenuation correction scheme based on path-integrated reflectivity is introduced. The precipitation attenuation coefficient is dynamically calculated point by point from the variation characteristics of real-time echo intensity along the beam path to compensate echo loss, which addresses the limitation that fixed correction parameters cannot adapt to attenuation differences under variable rainfall intensities. Based on the Z-R power-law relationship, the radar echo-derived rainfall is inverted, using hourly measurements from dense ground-based rain gauges as the reference values, and precision is verified using the MB and RMSE—industry-standard meteorological evaluation metrics. Experimental results demonstrate that clutter suppression dominates RMSE reduction (7.37 to 1.91 mm/h). Beam blockage correction shows negligible impacts on RMSE and MB. Attenuation correction delivers marginal MB improvement (−0.52 to −0.51 mm/h) with no measurable RMSE

Check for updates

Academic Editor: Merhala Thurai

Received: 31 July 2026
Revised: 18 September 2026
Accepted: 19 September 2026
Published: 21 September 2026

response. After full-chain quality-control optimization, the aggregate RMSE between radar-derived rainfall and gauge observations is 1.91 mm h^{-1}, representing an approximately 74% reduction compared with the raw dataset (from 7.37 to 1.91 mm h^{-1}). Elevated RMSE values of 4.2–5.0 mm h^{-1} are observed for rainfall intensities between 5 and 10 mm h^{-1}. In addition, the discrepancy between radar and gauge estimates grows as rainfall intensity increases. As the distance between radar and rain gauge increases, radar QPE systematically underestimates light precipitation, while persistent underestimation occurs across all ranges for heavy rainfall. This study enhances the differentiated quality control framework for X-band radar systems in complex mountainous regions, effectively improves the observation quality of radar-derived base data, and provides data support and technical references for dynamic monitoring of flash floods in mountainous river basins.

Keywords: X-band rainfall radar; ground clutter suppression; beam blockage correction; rain-attenuation correction; data quality control; quantitative precipitation estimation

1. Introduction

The intensity of X-band radar echo signals is influenced by various factors, including raindrop size, number density, and raindrop shape [1]; these signals can accurately reflect the characteristics of precipitation particles and serve as the core detection equipment for short-term rainfall observation. They are widely applied in various operational scenarios, such as rainfall type identification [2], rainfall monitoring [3,4], and flood simulation [5], and have become an essential data source for the construction of water resource digital twins, flood forecasting, and early warning systems, with multiple application cases observed along the Yellow River [6], Poyang Lake [7], Haihe River and Huaihe River [8], and Yongding River [9]. The radar detection signals undergo hardware processing to be converted into base data containing the echo reflectivity intensity Z. During linear propagation, the signals inevitably encounter interference from electromagnetic waves (originating from other radars, communication systems, large-scale mechanical operations, remote controllers, etc.), obstruction by ground objects (such as buildings, tall trees, wind turbines, etc.), or terrain obstructions; additionally, during periods of heavy rainfall, raindrops absorb a significant amount of X-band electromagnetic wave energy, leading to signal attenuation. The farther the signal travels from the radar, the more severe the signal attenuation becomes [10]. Therefore, before being deployed for practical applications, radar base data must undergo rigorous data quality control, which includes interference clutter removal, terrain obstruction correction, path attenuation correction, and rainfall intensity attenuation correction. The X-band water resources rainfall measurement radar is a type of Doppler radar operating at relatively short wavelengths; compared with Doppler radars using longer wavelengths, it offers higher spatial resolution, features a smaller antenna size and superior mobility, and has a lower cost. However, precisely because the wavelength in the X-band is relatively short, X-band hydrometeorological rainfall radar systems are more susceptible to interference from external sources—ranging from small atmospheric particles and flying birds to large obstacles such as mountains and buildings—which can generate false meteorological echoes. Hubbert et al. proposed a real-time ground clutter discrimination algorithm based on fuzzy logic; addressing the limitation of conventional radar-based full-field clutter filtering that may distort slow-moving meteorological echoes, this algorithm incorporates reflectivity variation characteristics and clutter phase alignment features to accurately localize clutter regions, thereby effectively eliminating ground clutter contamination while preserving authentic precipitation signals intact [11]. Su Tianji et al. employed a radial baseline noise extracted via fitting the root mean square error approach at the digital signal processing stage to suppress electromagnetic interference clutter, and they utilized radial interference identification combined with sequence autocorrelation techniques to filter out electromagnetic interference clutter from radar base data [12]. Bech et al. proposed a simple interception function between radar beams and topography for beam-blockage correction [13]. This method is generally robust under standard atmospheric propagation conditions, yet it yields substantial discrepancies under extreme anomalous propagation conditions. Fuzzy-logic radar quality-control schemes [14] are widely adopted to discriminate meteorological echoes from non-meteorological contaminants, including ground clutter and anomalous-propagation (anaprop) artifacts. Berenguer et al. [14] constructed the classifier from volumetric reflectivity features without polarimetric measurements. Research indicates that X-band radars are more vulnerable to path attenuation and rainfall intensity attenuation compared to long-wavelength radars [15]. Park et al., building upon an earlier developed data consistency analysis algorithm for C-band radars, derived a data consistency analysis methodology tailored for X-band radars and applied it to perform rainfall intensity attenuation correction [16]. If there is no rain intensity attenuation correction, even for light rainfall in stratiform clouds, X-band hydrometeorological rainfall radar can severely underestimate the rain intensity within a 10-km radius of the radar station [17]. Zhang et al. conducted research on radar echo attenuation correction algorithms, deriving a per-ensemble algorithm for attenuating correction based on integrated sampling observations of radar reflectivity factor data, and performed experiments to validate this approach [18]. A large number of researchers have proposed improvements to algorithms for X-band radar clutter suppression, beam occlusion correction, and rain attenuation correction [19]; however, most of their focus has been on investigating the impact of precipitation types or conducting experiments in flat terrain conditions, while research dedicated to quantitative precipitation estimation under complex terrain conditions remains relatively limited.

Li et al. have improved the quantitative precipitation estimation (QPE) algorithm for C-band weather radars by addressing aspects such as radar detection data quality control, terrain occlusion, the Z-R relationship, and radar mosaic integration in complex terrains; however, X-band rain measurement radars face multiple noise sources and complex attenuation influencing factors, meaning that the research results obtained for the C-band cannot accurately reflect the rain measurement performance of X-band radars [20]. In complex mountainous regions—particularly those with intricate ravine networks—where topographic undulations are significant, numerous first-order reflections and second-order multipath reflections inevitably occur during signal propagation. Compared with flat terrain areas, meteorological clutter and ground clutter exhibit deeper mixing, making it more challenging to distinguish between them. Regarding attenuation correction, when using dual-polarization parameters—such as the differential propagation phase and differential propagation phase shift—which are insensitive to path attenuation, echo position and echo intensity may easily be misaligned due to reflection phenomena. The research from Ramanamahefa et al. highlighted that the accuracy of the X-band radar QPE is strongly influenced by local topography [21]. Overall, there remains a substantial research gap in evaluating the accuracy of X-band radar rain measurement in complex terrains. This study focuses on complex mountainous areas where the elevation difference across the terrain exceeds 1000 m, selects rainfall scenarios with valid radar observations, and implements a comprehensive data quality control chain encompassing suppression of ground clutter—suppression of electromagnetic interference—correction for terrain occlusion—and correction for rain intensity attenuation; furthermore, an appropriate rain intensity inversion model is employed to convert the processed radar echoes into rainfall data. By comparing the processed rainfall data with measurements from nearby rain gauges, this study evaluates the accuracy of X-band water resources rain measurement radars in complex mountainous regions and provides data-driven support for improving data quality control methodologies.

2. Data and Research Methods

2.1. Data

2.1.1. X-Band Rainfall Radar

The base data used in this study were obtained from an X-band rainfall measurement radar, with its relevant parameters shown in the Table 1 below. The radar undergoes regular calibration to maintain measurement accuracy. No obvious anomalies of radar observations are identified from the data status. Although the radar is a dual-polarization system, only reflectivity data are utilized in this study. The radar system underwent routine factory calibration, and post-event checks confirmed no large absolute reflectivity bias during the observation period.

Table 1. The parameters of X-band radar.

Attribute	Attribute Value
frequency	9.1~9.5 GHz
antenna height	1065 m
wavelength	3.2 cm
beam width	1°
resolution of each range	150 m
the number of range gates	1000
azimuth range	360° (scan interval: 1°)
elevation	12 angles (0.5, 1.0, 1.5, 2.0, 2.5, 3, 3.5, 4, 5, 6, 7, 8)
volume scan interval	5 min

The data can generally be represented as a three-dimensional array $R^{12\times360\times1000}$ (representing 12 elevation angles, 360 azimuths, and 1000 range points). It should be noted that the radar yields no valid observations within the first 150 m (blind zone); thus, our valid range starts beyond this distance. Although the raw dataset contains 1000 range gates, only data within 60 km are retained for analysis, corresponding to the first 400 range gates. For subsequent research, 66 X-band volume-scan datasets from typical rainfall scenarios were selected. These observations have a temporal resolution of 5 min, covering the period from 20:00 UTC on 30 September to 02:00 UTC on 1 October 2025. This time window was chosen because gauge records indicate widespread rainfall across the study domain, providing abundant valid observational data for analysis. The schematic diagrams of two sets of observation results at an elevation angle of 0.5° are shown in Figure 1.

2.1.2. Digital Elevation Model (DEM) Data

The Copernicus Digital Elevation Model (Copernicus DEM, abbreviated as COP-DEM) is a global open-source topographic dataset released by the European Space Agency (ESA) under the framework of the "Copernicus Earth Observation Programme"; its GLO-30 version provides a spatial resolution of 30 m (approximately 1 arcsecond), enabling a detailed representation of surface undulations. These data are stored in GeoTIFF format, with each pixel containing attribute information such as longitude, latitude, and elevation, allowing for an accurate reflection of the absolute elevation of ground structures, vegetation canopies, and bare ground surfaces. In practical weather radar applications, radars perform three-dimensional scanning using polar coordinates (zenith angle, azimuth, and range), whereas DEM data are based on a geographic coordinate system (longitude–latitude grid);

thus, their spatial reference frames are fundamentally different. To enable precise terrain occlusion analysis centered around radar stations, DEM data were resampled onto the radar's polar coordinate grid through coordinate mapping and spatial interpolation. The radar polar coordinates are first converted to Cartesian plane coordinates, which are then transformed into WGS-84 geographic latitude and longitude. Subsequently, the elevation of each corresponding point is obtained via linear interpolation based on digital elevation model (DEM) data. Figure 2 presents surface–elevation data centered on the radar, which is located at (109.3° E, 34.1° N). with an elevation of 1065 m. Figure 2a presents the digital elevation model in WGS84 coordinates with a 1 km spatial resolution, while Figure 2b illustrates the radar-centered digital elevation model in polar coordinates (1° azimuth and 150 m range resolution).

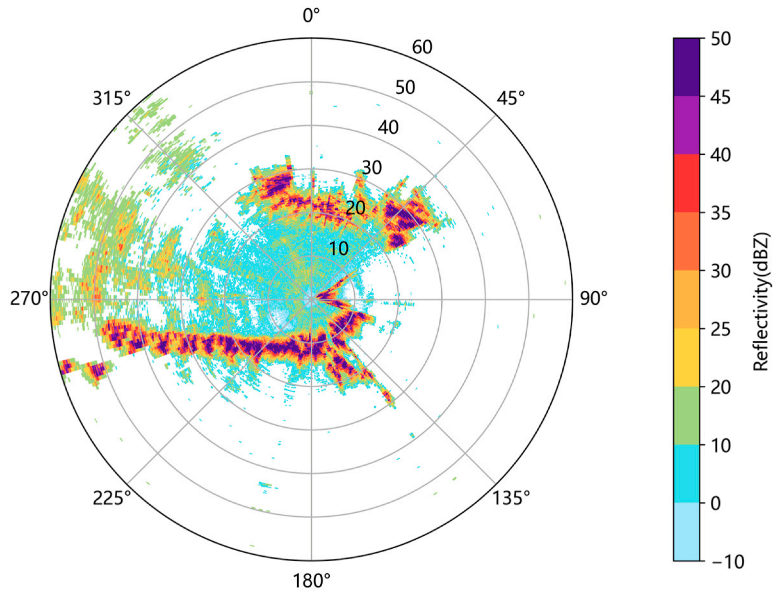

(**a**)

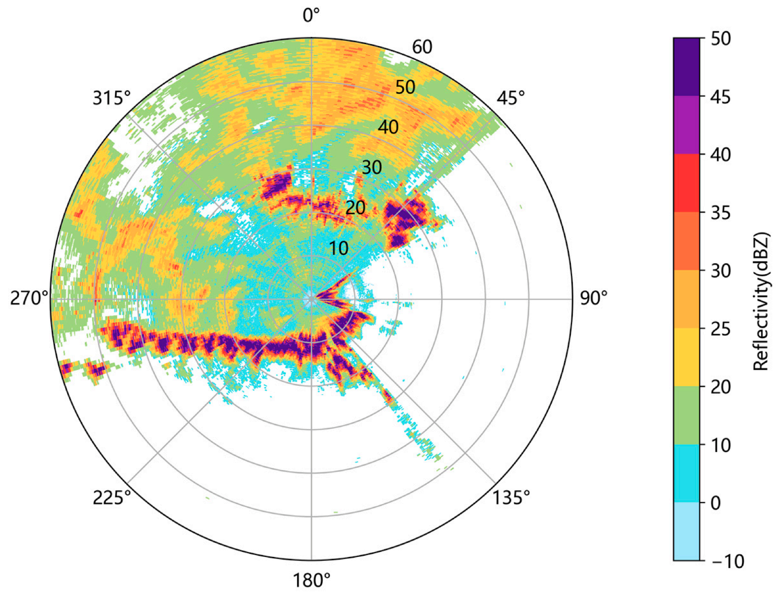

(**b**)

Figure 1. Examples of radar reflectivity data before quality control at an elevation angle of 0.5° (**a**) during the non-precipitation period (03:00 UTC, 15 August 2025); (**b**) during the precipitation period (23:30 UTC, 30 September 2025) (the circular rings denote points with equal slant range from the radar, and the numbers labeled on the rings represent slant distances in kilometers).

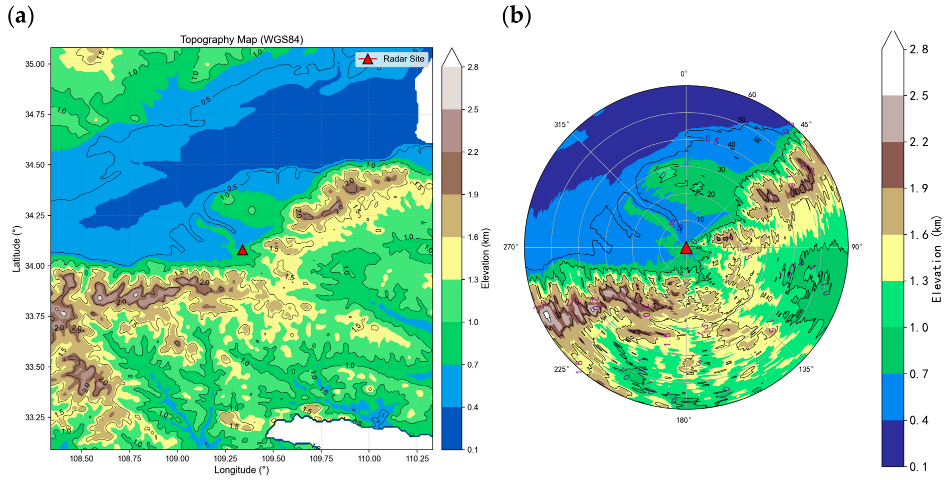

Figure 2. (**a**) Digital elevation model in WGS84 coordinates at 1 km spatial resolution; (**b**) radar-centered digital elevation model in polar coordinates (1° azimuth, 150 m range resolution). Circular rings represent constant straight-line distances from the radar, and ring labels show distances to the radar (km). Red triangle denotes the radar-site location.

2.1.3. Rainfall Station Monitoring Data

Hourly rainfall monitoring data within a 60 km radius of radar stations during the rainfall period were collected, including the station's longitude, latitude, hourly rainfall amounts, and rainfall occurrence times. A total of 410 ground-based rain-gauge stations were employed. Binary flags are defined for quality control purposes: 0 for invalid observations and 1 for valid observations. The rain-gauge stations within a 60 km radius of the radar station is shown in Figure 3.

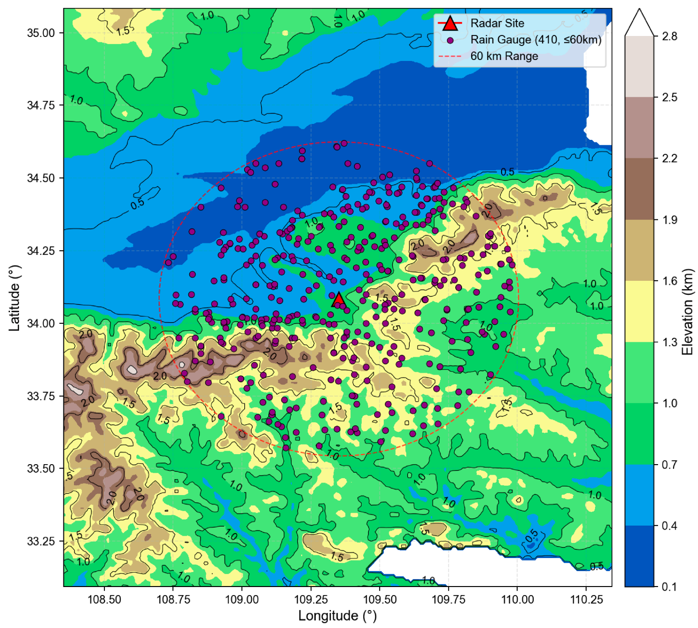

Figure 3. The rain-gauge stations within a 60 km radius of the radar station. Red triangle denotes the radar-site location.

2.2. Research Technique

The raw polar coordinate volume scan data from radar systems contain a large number of invalid echoes that hold no meteorological significance; these can be broadly categorized into two types: one consists of low-intensity clutter generated by instrument noise or weak atmospheric scattering; the other consists of false echoes produced by non-precipitation scatterers such as ground objects, radio frequency interference, and flying birds or insects. If such data are not pre-filtered out, it will significantly increase the computational errors encountered during subsequent beam obstruction correction, rain intensity attenuation correction, and rainfall inversion; furthermore, it may generate large areas of false rainfall pixels, thereby interfering with the identification of rainfall conditions. Therefore, it is necessary to set a reflectivity threshold to perform basic filtering of non-precipitation echoes. The unit for radar reflectivity is dBZ, and the numerical value directly represents the equivalent reflectivity strength of the scattering particles. When only trace amounts of water vapor, aerosols, or dust exist in the atmosphere, the scattering energy is extremely low, and the corresponding reflectivity values are generally below 0 dBZ; echoes within this range cannot represent effective rainfall. Consequently, a uniform threshold of 0 dBZ is set as the baseline screening criterion, and this threshold screening process is applied to all radial distance datasets and all elevation-layer data: the entire radar radial distance dataset is traversed, and any pixel with a reflectivity value less than 0 dBZ is directly marked as an invalid value and excluded from further quality control and quantitative rainfall inversion processes.

The raw radar dataset comprises a series of volume scans, with each scan containing observations acquired at 12 elevation angles. Layer-wise quality-control procedures, including ground clutter suppression, terrain-induced beam blockage correction and rain attenuation correction, are implemented for every elevation slice. Linear interpolation resampling is adopted to project polar-coordinate radar data onto a geographic grid, generating a 12-layer 3D reflectivity field with a horizontal resolution of 0.0015°. Composite reflectivity for each grid cell is obtained by taking the vertical maximum reflectivity across all elevation layers. Gridded radar rainfall is retrieved from composite reflectivity using the Z-R relationship. Using 1 h rain-gauge observations, radar rainfall values at gauge locations are extracted via nearest-neighbor sampling under a temporal tolerance of 5 min. The matched gauge–radar pairs are constructed for quantitative statistical evaluation. The detailed process is listed in Algorithm 1:

Algorithm 1: Radar-derived QPE processing and gauge–radar matching

```
Input: Raw radar volume scan dataset, 5-min rain-gauge observations
Output: Gridded radar rainfall dataset, matched gauge–radar pairs
(1) FOR each radar volume scan:
    // Quality control for 12 elevation layers
    FOR each elevation angle (12 layers in total):
        Perform layer-wise quality control:
            (1) ground-clutter suppression
            (2) terrain-induced beam-blockage correction
            (3) rainfall attenuation correction
    END
    // Linear interpolation resampling from polar to geographic grid
    Map polar-coordinate radar data to the WGS-84 geographic grid
    via linear interpolation, generating a 12-layer 3D reflectivity field
    with a horizontal resolution of 0.0015°.
    // Calculate composite reflectivity
    FOR each grid cell:
        Composite reflectivity = maximum reflectivity across all 12 elevation layers
    END
```

Algorithm 1 *Cont.*

// Retrieve gridded rainfall via Z-R relationship
Gridded radar rainfall = Z-R transformation (composite reflectivity)
END
(2) Spatiotemporal matching:
FOR each 1 h rain-gauge observation:
Extract radar rainfall at gauge location via nearest-neighbor resampling
under a temporal tolerance of 5 min.
Construct matched gauge–radar sample pairs.
END
(3) RETURN Gridded radar rainfall, matched gauge–radar pairs

2.2.1. Clutter Suppression Index

Terrain clutter originates from echoes reflected by static terrain features such as mountains, buildings, transmission towers, and vegetation; it is characterized by fixed positions and stable temporal patterns, making it the primary source of interference for radar systems. Currently, methods that combine multiple features for terrain interference suppression are widely adopted [11]. This study primarily employs the following indicators.

(1) Reflectance factor level texture T_{dBZ}

$$T_{\text{dBZ}} = \frac{\sum_{i=1}^{N_A}\sum_{j=1}^{N_R}\left(Z_{i,j} - Z_{i,j+1}\right)^2}{N_A \times N_R}$$

In the formula, i denotes the azimuthal index, j denotes the range index, N_A and N_R represent the total number of samples in the azimuthal and range directions, respectively; typically, N_R = 3 and N_A = 3. The T_{dBZ} value reflects local variations in echo intensity: terrain clutter exhibits relatively high T_{dBZ} values due to the non-uniform distribution of scatterers, whereas precipitation echoes are relatively smooth.

(2) Vertical variation of the reflectivity factor (G_{dBZ})

$$G_{\text{dBZ}} = \left(Z_{\text{up}} - Z_{\text{low}}\right)$$

Z_{up} and Z_{low} denote the reflectivity factors for the upper and current layers, respectively. In this calculation, the range-dependent weighting function W(R) is omitted. This simplification assumes that range-related differences in echo power are negligible within our 60 km maximum radar range, so the range weighting term exerts little influence on the final G_{dBZ}. Ground clutter exhibits relatively large negative G_{dBZ} values because it occurs exclusively in the lower layer, whereas the absolute G_{dBZ} values of precipitation echoes are smaller.

(3) Radial variation of the reflectivity factor: *SPIN*

$$SPIN = \frac{\sum_{i=1}^{N_A}\sum_{j=1}^{N_R} M_{SPIN}}{N_A \times N_R}$$

$$M_{SPIN} = \begin{cases} 1 & \mid Z_{i,j} - Z_{i,j-1} \mid > Z_{\text{thresh}} \\ 0 & \mid Z_{i,j} - Z_{i,j-1} \mid \leqslant Z_{\text{thresh}} \end{cases}$$

The Z_{thresh} value is typically set between 2 and 5 dB. The *SPIN* parameter reflects the degree of variation in the reflectivity factor along the radial direction; objects with surface clutter exhibit a higher *SPIN* value.

(4) Time variance *TVAR*

The reflectivity time variance is the most direct indicator for measuring the degree of dispersion in a reflectivity sequence. For stationary targets, the reflectivity remains nearly constant over time; consequently, its time variance is close to the radar's measurement noise variance. In contrast, meteorological echoes exhibit significant time variances due to the formation and dissipation of precipitation, advection, and intensity fluctuations. The time variance at a single grid point is defined as:

$$TVAR = \frac{1}{N-1}\sum_{k=1}^{N}(Z_k - \bar{Z})^2$$

Here, Z_k denotes the reflectivity at time step k (dBZ).

$$\bar{Z} = \frac{1}{N}\sum_{k=1}^{N} Z_k$$

In this experiment, four features—T_{dBZ}, G_{dBZ}, $SPIN$, and $TVAR$—are employed for target interference identification and removal. If either all of T_{dBZ}, G_{dBZ} and $SPIN$ conditions (texture features) are satisfied or the $TVAR$ condition (temporal feature) is satisfied, the corresponding data point is labeled as clutter; after filtering, further processing is performed. For the dataset $R^{12\times360\times400}$ acquired by an X-band radar, T_{dBZ}, G_{dBZ}, $SPIN$, and $TVAR$ are computed for each data point following the specified formulas. In this experiment, the thresholds for target echo identification were set as $T_{\mathrm{dBZ}} > 20$, $G_{\mathrm{dBZ}} < -6$, $SPIN > 0.15$ (valid when $Z_{\mathrm{thresh}} = 3$), and $TVAR < 25$, which were calibrated from experiments conducted on an independent dataset from 15 August 2025.

Electromagnetic interference originates from communication base stations, power transmission lines, wind turbine blades, industrial RF equipment, adjacent radar systems with identical frequency signals, etc.; it typically exhibits an isolated point-like, linear, or radial strip-like discrete distribution, with very few cases where large-scale continuous sheet-shaped echoes are formed. The azimuth and range distributions show no fixed patterns and do not follow the terrain contour (distinguishing them from terrain clutter); furthermore, there are no coherent echoes along adjacent radial directions within the same distance bin. The intensity undergoes abrupt and sharp transitions, with significant differences in reflection coefficients between preceding and succeeding radial distance bins, often resulting in sudden peaks of extremely high values (ranging from 40 to 60 dBZ); there is no gradual transition between strong and weak signal levels, unlike real rainfall, which features a central strong echo followed by a smooth attenuation outward. In some cases, narrowband interference manifests as abnormally high values only at a few specific distance bins, while other positions exhibit only noise. Given that the suppression of electromagnetic interference clutter exhibits radial distribution characteristics, this experiment employs two features—T_{dBZ} and $SPIN$, which are commonly used in ground-clutter suppression identification—to perform the identification and removal process. Electromagnetic interference suppression should be introduced separately from ground-clutter suppression, even though both can be identified using texture-based features. This is because they originate from distinct physical mechanisms.

2.2.2. Beam-Blockage Correction

Following the methodology of the Beijing Meteorological Bureau, and by fully accounting for the effects of Earth's curvature and standard atmospheric refraction, a beam-blockage correction is conducted [22]. First, the low-altitude detection altitude of the radar beam is calculated; this altitude refers to the height above ground at which the radar beam, operating at its minimum working elevation angle, strikes the lower edge of the beam as it illuminates a target at a specific distance. If the low-altitude detection altitude exceeds the terrain elevation, no beam blockage exists. Conversely, if the low-altitude detection altitude is below the terrain elevation, beam blockage occurs, necessitating further beam blockage analysis to compute the actual beam occlusion rate. The formula for calculating the radar's low-altitude detection altitude is as follows:

$$b_{\mathrm{h}} = \sqrt{(R_{\mathrm{E}}+\mathrm{h})^2 + r^2 + 2r(R_{\mathrm{E}}+\mathrm{h})\sin(\varphi - \theta_{3\mathrm{dB}}/2)} - R_{\mathrm{E}} - \mathrm{h}$$

In the formula, $\mathrm{b_h}$ denotes the low-altitude radar detection altitude; $\mathrm{R_E}$ denotes the Earth's effective radius, with a value of 8500 km; h denotes the elevation height of the antenna feed; r denotes the radar detection range (all distances are expressed in km); φ denotes the radar operating elevation angle; and $\theta_{3\mathrm{dB}}$ denotes the radar beam width (all units are °).

Beam blockage analysis is conducted for each radar beam. For each azimuth angle, divide the range from −1.5° to 1.5° into 31 azimuth points (with a resolution of 0.1°) to perform cumulative calculations; the weather radar beam occlusion rate O is then calculated using the specified formula.

$$O = \sum_{n=-15}^{15} B_{LE(n)} W_{A(|n|)}$$

In the formula, O denotes the occlusion rate; BLE(n) represents the electromagnetic wave beam blockage rate at the n-th azimuth angle; $\mathrm{W_{A(|n|)}}$ indicates the beam offset attenuation coefficient at the n-th azimuth angle.

$$W_{A(|n|)} = \frac{\int_{0.1(|n|-0.5)}^{0.1(|n|+0.5)} exp\left[-4\ln 2(\theta/sig)^2 \mathrm{d}\theta\right]}{\int_{-1.55}^{1.55} exp\left[-4\ln 2(\theta/sig)^2\right]\mathrm{d}\theta}$$

sig denotes the weather radar beam width; n ranges from −15 to 15.

At the n-th azimuth angle, if there is no beam blockage within the ±1.5° elevation angle offset range, then $B_{LE(n)} = 0$. If beam blockage occurs at m consecutive elevation angle offsets starting from an elevation angle offset of −1.5°, BLE(n) is computed as follows:

$$B_{LE(n)} = \frac{\int_{-1.55}^{0.1(\mathrm{m}+0.5)} exp\left[-8\ln 2(\theta/sig)^2 \mathrm{d}\theta\right]}{\int_{-1.55}^{1.55} exp\left[-8\ln 2(\theta/sig)^2\right]\mathrm{d}\theta}$$

m ranges from −15 to 15.

The partial-beam-blockage fraction (PBB) was computed for the study domain, and the results are presented in Figure 4. The partial-beam-blockage (PBB) fraction map in polar coordinates corresponds to elevation angles of 0.5° (left panel) and 1° (right panel).

As illustrated, partial beam blockage occurs at certain azimuths and ranges for the 0.5° elevation angle, with PBB values exceeding 50% in some regions. At the elevation angle of 1°, beam-blockage fractions decrease substantially and remain mostly below 10%. Further reduction in blockage is observed at 1.5°, where most areas experience no terrain-induced beam blockage. For elevation angles above 1.5°, beam blockage is absent across the entire domain.

In complex mountainous regions, improving the spatial resolution of topographic data helps enhance the accuracy of beam blocking correction [23]. This study employs topographic data with a spatial resolution of 30 m, which represents an improvement compared to the 250 m resolution data used by Yu et al. [23]. First, the occlusion rate is calculated, followed by compensation based on the beam blocking correction rules adopted by the Beijing Meteorological Bureau. If the terrain-induced partial-beam-blockage fraction (PBB) for a given elevation angle is less than 60%, the radar echo is retained for further processing, and the reflectivity factor at this elevation angle is corrected using the corresponding formula. When PBB greater than 60% [24], the beam is regarded as fully blocked, forming a radar blind zone.

$$\Delta Z = -10 \log_{10}(1 - O)$$

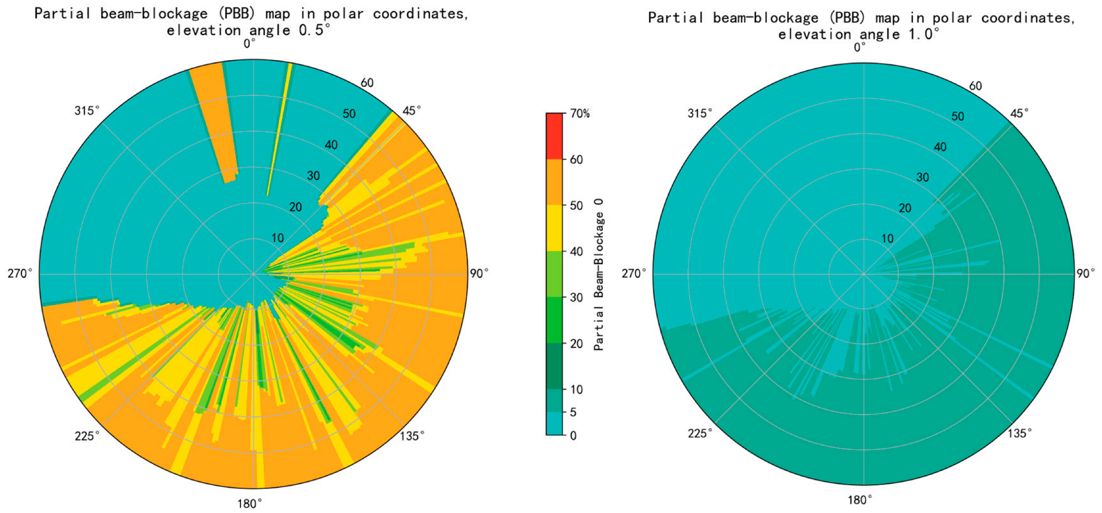

Figure 4. Partial-beam-blockage (PBB) fraction map in polar coordinates for the elevation angle of 0.5° (**left**) and 1° (**right**). Color bar denotes partial-beam-blockage fraction (%). The concentric circular rings represent distances from the radar site.

2.2.3. Rain-Induced Attenuation Correction

Due to their short wavelengths, X-band rain-measuring radars experience signal attenuation when passing through rain zones, which severely impacts the application of radar data [25]. Therefore, it is essential to perform attenuation correction on the radar data prior to its utilization. The attenuation correction of weather radar reflectivity factors is primarily achieved by leveraging the relationship between the attenuation rate and the reflectivity factor. The empirical relationship between the attenuation coefficient $\kappa(R)$ and the radar reflectivity factor Zr(R) can be expressed as follows:

$$\kappa(R) = aZ_r^b(R)$$

$$Z_r(R) = Z_m(R)exp\left\{2\int_0^R aZ_r^b(R)\mathrm{d}R\right\}$$

$Z_r(R)$ denotes the true intensity (true value) of the radar reflectivity factor for the Rth range bin, while the corresponding measured intensity (measured value) is denoted as such $Z_m(R)$. The X-band radar operates at frequencies of 9.1–9.5 GHz, corresponding to a nominal wavelength of 3.2 cm, where a = 3.0199 × 10^{-9}, b = 0.8771, and $\kappa(R)$ is given in units of Np/m [18]. In this experiment, the sequential range bin correction method proposed by Zhang et al. was employed for attenuation correction [18]. The attenuation correction is applied sequentially along the radial direction to each range bin: after completing the attenuation correction for the i-th range bin, the parameter τ_i is calculated using the corrected results from the first i range bins, followed by performing the attenuation correction for the (i + 1)-th range bin, as described below:

$$\tau(R) = exp\left\{-2\int_0^R \kappa(R)\mathrm{d}R\right\}$$

$$Z_r(i) = [Z_m(i)/\tau_{i-1}]exp\left\{a[Z_m(i)/\tau_{i-1}]^b \Delta R\right\}$$

ΔR denotes the distance resolution; i represents the index of the range bin, with values ranging from 1 to 1000; and τ_i represents the rainfall intensity attenuation coefficient for the i-th range bin. Although the X-band radar used in this study provides complete dual-polarization observations, the current work mainly focuses on the performance of reflectivity-only attenuation correction. Polarimetry-based attenuation correction is not used here.

2.2.4. Precipitation Inversion

The classical Z-R relationship is employed for quantitative precipitation estimation [26], wherein the radar echo intensity (dBZ) is converted into the reflectivity factor based on the relationship between echo intensity and the reflectivity factor.

$$\text{dBZ} = 10\text{lgZ}$$

Rainfall intensity inversion is performed based on the relationship between the reflectivity factor Z and rainfall intensity R.

$$\text{Z} = \text{A} \times \text{R}^{\text{b}}$$

In the formula, Z is the reflectance factor, with units of mm^6/m^3; R is the rainfall intensity, with units of mm/h; and A and b are inversion parameters. In this study, a = 200 and b = 1.6.

2.2.5. Statistical Method

The Bias (MB) quantitatively measures the degree of systematic overestimation or underestimation of radar-derived precipitation estimates relative to ground-based reference observations; its calculation formula is the mean of the differences between the radar estimates and the reference values. The Normalized Mean Bias (NMB) represents the relative systematic bias, defined as the ratio of the total bias to the sum of reference observations. NMB eliminates the influence of precipitation magnitude and facilitates cross-case comparison of systematic deviation under different rainfall intensities. The Root Mean Square Error (RMSE) measures the root mean square of the differences between the estimated values and the reference values, reflecting the absolute dispersion of the error. The calculation method is as follows:

$$\text{MB} = \frac{1}{N}\sum_{r=1}^{N}(R_r - G_r)$$

$$\text{NMB} = \sum_{r=1}^{N}(R_r - G_r)/\sum_{r=1}^{N}(G_r)$$

$$\text{RMSE} = \sqrt{\frac{1}{N}\sum_{r=1}^{N}|G_r - R_r|^2}$$

In this formula, N denotes the number of samples composed of radar-derived rainfall estimates and corresponding rain gauge measurements, while r is the index of paired radar-gauge samples; R_r represents the radar-derived rainfall estimate; and G_r represents the corresponding rain gauge measurement.

3. Results and Discussion

The results after ground clutter and electromagnetic interference are shown in Figure 5. As illustrated in the figure, high-value echoes within the azimuth sectors of 180–270° and 0–45° are identified as anomalies based on terrain analysis, and these echoes are completely removed by the algorithm. Although considerable valid echoes are discarded in this process, experimental results demonstrate that sufficient data remain available for subsequent analysis.

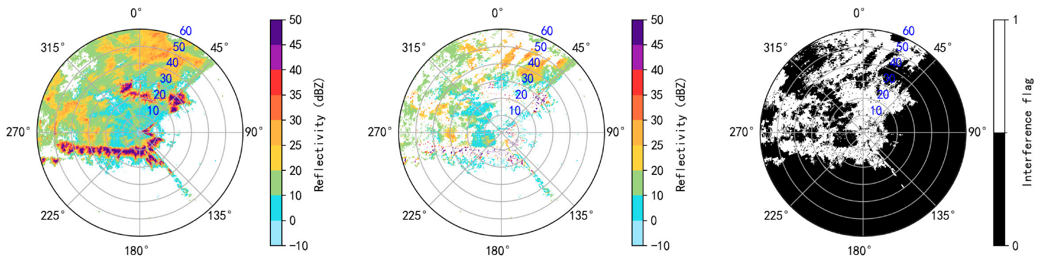

Figure 5. From left to right: radar reflectivity at an elevation angle of 0.5° before clutter suppression, radar reflectivity after clutter suppression, and the extracted clutter distribution, at 23:30 UTC on 30 September 2025. The plots are presented in radar-centered polar coordinates with an azimuth resolution of 1° and a range resolution of 60 m.

For typical rainfall periods, the following corrections are applied sequentially to data from each elevation-angle layer: ground-clutter suppression, electromagnetic interference suppression, beam-blockage correction, and attenuation correction for rainfall intensity. The corrected layer data are then interpolated from radar-centered polar coordinates to a regular latitude-longitude grid with a spatial resolution of 0.0015° under the WGS-84 coordinate system using linear interpolation. The processed radar echoes are used to compute composite reflectivity by taking the maximum value among all elevation-angle layers for each grid cell. Based on the composite reflectivity of each lat–lon grid, the rainfall-retrieval formula is adopted to convert reflectivity into radar-derived rainfall estimates, producing regular-gridded surface rainfall data with the same 5 min temporal resolution as the original radar echoes. Hourly rainfall observations from rain gauge stations are used. Radar-derived rainfall estimates matching the exact date-hour records are extracted at each gauge location via nearest-neighbor interpolation over the WGS-84 coordinate grid to construct statistical samples. For gauge–radar matching, the nearest-neighbor approach was adopted instead of small-neighborhood spatial averaging. Although neighborhood averaging can increase the number of valid matched samples when the nearest radar pixel is contaminated or missing, it introduces spatial smoothing and may distort the native radar-reflectivity features at fine scales. Given the complex mountainous terrain in the study area, sharp spatial gradients of precipitation frequently occur. To preserve the original spatial characteristics of radar-derived rain-rate fields, nearest-neighbor matching was therefore preferred in this work.

In our experiments, the total sample count decreased by 56% after quality-control processing relative to the raw dataset. We adopt a matched subset of collocated samples for statistical comparison of radar-derived hourly rainfall against gauge-observed rainfall, for both raw radar outputs and the outputs after each individual processing step. The spatial map of sample counts at a resolution of 0.1° is shown in Figure 6. It can be seen that the dataset nearly covers the entire target analysis domain, laying a solid foundation for subsequent experiments. The results for each individual processing step are presented in Figures 7–10. Radar reflectivity factors are extracted from raw base radar data using the same procedure adopted for the corrected dataset to generate the original radar rainfall estimates.

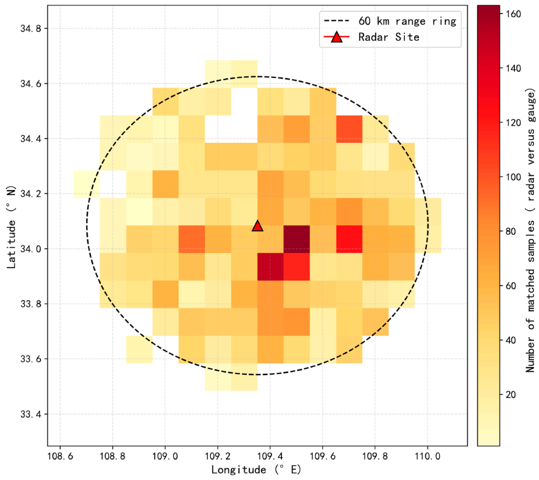

Figure 6. Spatial map of the number of matched samples (radar-derived hourly rainfall vs. gauge-measured rainfall).

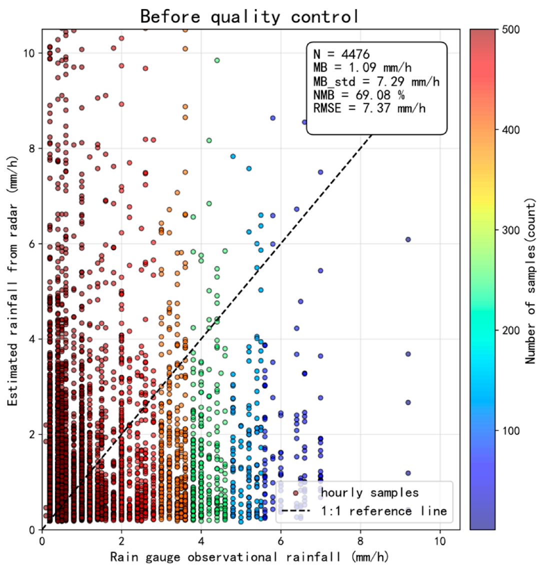

Figure 7. Statistical comparison of raw radar-derived hourly rainfall against gauge-measured rainfall.

As shown in the figures, nearly all of the RMSE reduction (7.37 to 1.91 mm/h) originates from clutter suppression. Beam-blockage correction slightly improves NMB, raising it from −32.81% to −32.74%, while RMSE remains unchanged. In contrast, attenuation correction has no effect on RMSE (Figures 8 and 9 are identical) and reduces bias from −0.52 to −0.51 mm/h. This indicates that clutter-suppression processing substantially improves radar-data performance, whereas beam-blockage correction yields limited reduction in NMB. Rain-attenuation correction brings slight improvement, as reflected by the NMB changing from −32.74% to −32.45%. After sequential clutter suppression, beam-blockage correction and rain-attenuation correction, the aggregate RMSE is reduced by approximately 74% (from 7.37 to 1.91 mm h^{-1}) relative to the pre-quality-control dataset. Meanwhile, the magnitude of MB drops to 47% of its original value, demonstrating considerable improvement in data quality. In addition, the quality-control procedure removes numerous spurious high-rainfall observations.

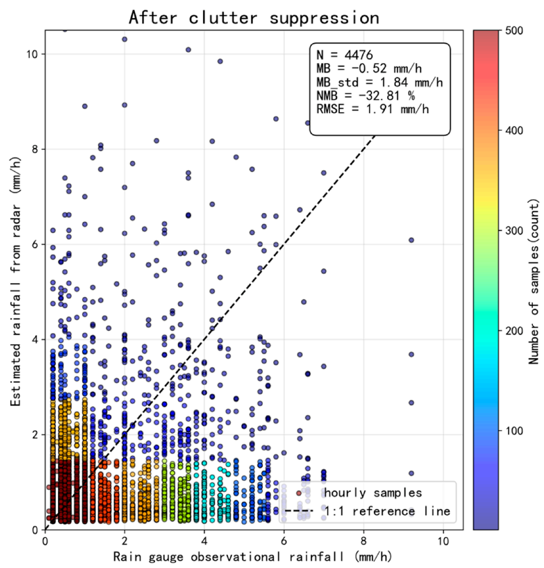

Figure 8. Statistical comparison of radar-derived hourly rainfall after clutter depression against gauge-measured rainfall.

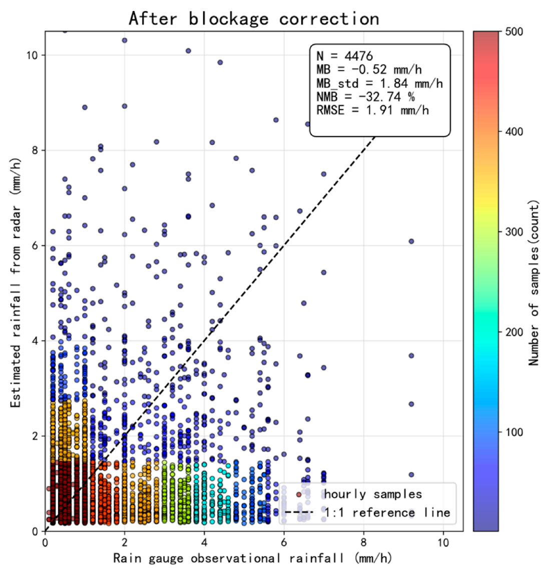

Figure 9. Statistical comparison of radar-derived hourly rainfall after clutter suppression and beam-blockage correction against gauge-measured rainfall.

According to the beam-blocking algorithm design, the maximum magnitude of beam-blockage correction reaches 4 dBZ. Nevertheless, discrepancies between radar-derived rainfall and rain-gauge observations show no obvious reduction (MB remains −0.52mm/h) after beam-blockage correction, which indicates limited effectiveness for this correction step. This phenomenon mainly arises because samples suffering from severe beam blockage are eliminated in the filtering procedure; the remaining samples only feature moderate blockage, and the missing information is largely compensated by observations from higher-elevation radar scans. For rain-induced attenuation correction, in simulation experiments performed at the same range resolution as the radar described in this study, under the condition of continuous radar signals, the magnitude of rain attenuation-correction increases with increasing range and radial echo intensity and can exceed 20 dBZ or even higher. In other published studies, the magnitude of rain-induced attenuation correction can exceed 10 dBZ for mountain-located X-band radars [27]. Nevertheless, without echo filling, the correction magnitude in our experiments is mostly below 1 dBZ, and the processed results show little difference from those obtained by beam-blockage correction alone. This is attributed to substantial missing echoes along radars after signal filtering. Filling missing regions with proper meteorological rainfall echoes may yield substantially larger correction magnitudes, which should be studied further in future work. Existing studies indicate that no single parameter combination can be consistently effective for attenuation correction and highlighted the need for event- and radar-specific attenuation correction [21].

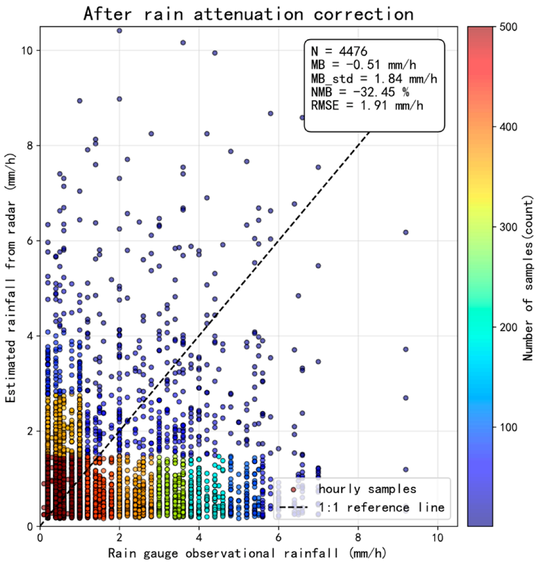

Figure 10. Statistical comparison of radar-derived hourly rainfall clutter suppression, beam-blockage correction and rain attenuation correction against gauge-measured rainfall.

The quality-controlled matched samples were grouped by distance bins of 0–10 km, 10–20 km, 20–30 km, 30–40 km, and 40–60 km. The RMSE was calculated for rainfall rates binned by rain-gauge observations, including the 0–5 mm/h and 5–10 mm/h categories, as listed in Table 2. There were insufficient matched samples for rainfall rates of 10–20 mm/h and 20–40 mm/h in this dataset; hence, statistical evaluation for moderate-to-heavy rainfall could not be conducted, which constitutes a limitation of this study.

Table 2. Statistical Analysis of discrepancies between radar-derived rainfall and rain-gauge measurements (unit: mm/h).

Rainfall Distance	0~5 mm/h					5~10 mm/h				
	RMSE (mm/h)	MB (mm/h)	MB_STD (mm/h)	NMB (%)	N	RMSE (mm/h)	MB (mm/h)	MB_STD (mm/h)	NMB (%)	N
0~10 km	1.04	0.02	1.05	1.63	122	-	-	-	-	-
10~20 km	1.44	−0.05	1.44	−3.68	663	4.24	−4.18	0.83	−83.7	3
20~30 km	1.56	0.11	1.56	10.81	871	4.5	−4.06	1.95	−69.59	64
30~40 km	1.59	−0.33	1.55	−24.64	804	4.35	−2.82	3.39	−51.57	25
40~60 km	1.78	−0.64	1.66	−41.24	1794	4.99	−4.63	1.87	−77.01	130

Note: The symbol "-" in the table indicates insufficient sample size to perform statistical analysis.

The table indicates that for light rainfall (0–5 mm/h), the RMSE increases gradually with range, rising from 1.04 mm/h (0–10 km) to 1.78 mm/h (40–60 km). Within the 0–30 km range, the radar exhibits slight systematic overestimation: the mean bias (MB) is 0.02 mm/h for 0–10 km, −0.05 mm/h for 10–20 km, and 0.11 mm/h for 20–30 km, with corresponding NMB values of 1.63%, −3.68%, and 10.81% (positive NMB denotes overestimation). Beyond 30 km, the bias shifts to systematic underestimation: the MB falls

https://doi.org/10.3390/atmos17090912

to −0.33 mm/h (30–40 km) and further to −0.64 mm/h (40–60 km), accompanied by NMB values of −24.64% and −41.24%, respectively, showing that the underestimation becomes stronger as range increases beyond 30 km.

For moderate rainfall (5–10 mm/h), the overall error is substantially larger than for light rainfall. The RMSE ranges from 4.24 mm/h (10–20 km) to 4.99 mm/h (40–60 km), which is more than twice the RMSE for light rainfall. The radar shows severe systematic underestimation across all valid distance bins for this rainfall category, with consistently negative MB values: −4.18 mm/h (10–20 km), −4.06 mm/h (20–30 km), −2.82 mm/h (30–40 km), and −4.63 mm/h (40–60 km). All NMB values are below −50%, meaning the radar underestimates moderate rainfall relative to gauge observations. The strongest underestimation appears at 10–20 km (NMB = −83.70%), and the mildest underestimation occurs at 30–40 km (NMB = −51.57%).

Our results reveal that radar precipitation retrieval performance is highly sensitive to rainfall intensity. Light rainfall (0–5 mm/h) yields much lower overall errors and relatively weak bias, whereas moderate rainfall (5–10 mm/h) is characterized by pronounced systematic underestimation and markedly elevated RMSE values across all valid distance ranges. Range also imposes notable impacts. For light rainfall, overestimation is observed within 0–30 km, while underestimation dominates at 30–60 km. For moderate rainfall, large errors persist at all available ranges, and underestimation is severe in the farthest 40–60 km bin.

Based on the experimental results, the overall MB value of −0.51 mm/h indicates that radar-derived rainfall generally underestimates rain-gauge observations. This underestimation is more pronounced under moderate-rainfall conditions (5–10 mm/h) compared with light-rain conditions (0–5 mm/h). The experiment revealed that the attenuation correction for rainfall intensity is significantly affected by extensive data gaps, resulting in relatively small correction magnitudes (0.1–0.3 dBZ). Echo filling would be a promising approach to address this problem; however, the strategy for performing the filling remains an open issue. At this experimental site, only the lowest elevation angle experiences significant terrain blockage, while other elevation angles are essentially free from terrain blockage; consequently, the magnitude of the beam-blockage correction is also limited. The observation that radar measurements at long distances yield low rainfall intensities suggests that the current correction approach is insufficient; therefore, it is necessary to implement amplification of the attenuation correction specifically for complex terrain conditions. The current method was originally proposed for long-waveband radars; its direct application to short-wavebands may cause a sharp increase in distortion within long-distance mountainous rainfall zones. Additionally, the natural energy attenuation of X-band radar echoes during propagation is more severe compared to that of C-band radar echoes; This may partly explain why radar-derived rainfall estimates tend to systematically underestimate actual rainfall from rain-gauge observations. Other potential error sources may also account for the observed bias, including the rule of data filtering, the underestimate in attenuation correction, the vertical sampling height difference between radar radar-beam observations and surface rain-gauge measurements, and the empirical fixed Z-R relationship [28].

4. Conclusions

X-band rainfall radar has emerged as a core observational tool for capturing small- and medium-scale precipitation in complex mountainous basins. Nevertheless, its raw echoes are subject to severe distortion, and their compatibility with conventional quality control and correction approaches remains limited, which often leads to low accuracy in quantitative precipitation estimation in mountainous regions. To address these engineering challenges, this study utilizes real-time time-series data from X-band rainfall radars deployed across mountainous areas to construct a quality control system that integrates clutter removal, electromagnetic interference suppression, beam blockage correction, and rain-induced attenuation correction. These findings indicate that clutter suppression is the dominant contributor to the overall reduction in RMSE (from 7.37 to 1.91 mm/h). By contrast, beam-blockage correction yields no change in RMSE and MB. Attenuation correction produces a marginal improvement in MB (from −0.52 to −0.51 mm/h) with no measurable change in RMSE. Furthermore, by leveraging the Z-R power-law relationship, the study derives rainfall estimates from quality-controlled radar echoes and employs measured data from high-density ground-based rain gauge stations to conduct quantitative accuracy verification across multiple indicators.

The experimental results demonstrate that the proposed quality-control system can effectively filter abnormally high reflectivity values induced by multi-source interference over mountainous terrain, significantly improve the consistency between radar-derived rainfall estimates and ground-measured rainfall values, substantially reduce both systematic errors and random errors in precipitation estimation, and effectively address the issues of raw echo distortion in X-band radars within complex mountainous areas and poor stability in precipitation estimation. However, comparative analysis of the experiments revealed that the radar-derived rainfall estimates across the study area generally fall below the measurements obtained from ground-based rain gauges; furthermore, this negative deviation exhibits a significant increasing trend as the rainfall intensity rises, highlighting notable limitations in the current correction system. The beam-blockage correction exhibits limited improvement in this case, which is likely attributed to the complementary observational coverage provided by higher-elevation radar scans. Additionally, the propagation of electromagnetic waves in X-band through rain zones experiences far more severe energy attenuation compared to that in C-band; during long-distance propagation along rainbands, the distortion of echo energy is continuously amplified, ultimately resulting in more pronounced underestimation of rainfall amounts for moderate precipitation conditions compared to light rain scenarios.

In summary, this study presents a feasible approach to mitigate data quality issues arising from the superposition of multiple interference sources for X-band radars in complex mountainous terrain. Owing to the topographic features of the radar site, low-level beams are frequently subject to terrain blockage in this region, which partly accounts for the satisfactory performance of the algorithm. Nevertheless, the parameters may require further tuning when applied to other regions. Furthermore, this study clarifies the adaptive limitations of conventional long-wavelength radar correction algorithms in X-band mountainous environments, identifies the dominant error sources for X-band radar precipitation estimation under heavy rainfall and long-range propagation conditions, and lays a solid foundation for subsequent targeted optimizations. Potential future work includes developing dedicated correction models for short-wavelength radars, improving attenuation compensation for heavy precipitation scenarios via KDP (Specific Differential Phase)-based or PIA (Path-Integrated Attenuation)-constrained approaches, and ultimately enhancing the quantitative precipitation estimation performance of X-band radars in complex mountainous terrain. It should be noted that this study is based on observations from a single X-band radar deployed in complex mountainous terrain. Caution should be exercised when extrapolating these findings to other mountainous regions, as topographic conditions exert substantial influences on X-band-radar rainfall estimations.

Author Contributions: X.L. (Xiaoning Li) contributed to the conceptual design of the work and drafted the manuscript for key intellectual content. Y.W. contributed to data acquisition, analysis and interpretation. X.L. (Xiaowan Liu) and B.Z. performed data analysis. Z.G. performed data analysis, investigation and visualization. M.X. provided supervision. All authors have read and agreed to the published version of the manuscript.

Funding: This work was supported by the Gansu Provincial Water Resources Science, Experimental Research and Technology Promotion Program of China, under the project entitled Research on Data Quality Control Methods of X-band Precipitation Radar for Mountain Flash Flood Early Warning (Grant No. 26GSLK129).

Institutional Review Board Statement: Not applicable.

Informed Consent Statement: Not applicable.

Data Availability Statement: The observations data are available when requested.

Conflicts of Interest: The authors declare no conflicts of interest.

References

1. Liu, X.; Huang, H.; Hu, S.; Xia, F.; Lai, R.; Feng, L.; Xiao, H.; Li, H.; Rao, X. Retrieval of Parameters of Constrained Gamma Raindrop Size Distribution in South China. *J. Hydrometeorol.* **2024**, *25*, 1747–1765. [CrossRef]
2. Ribaud, J.F.; Machado, L.A.T.; Biscaro, T. X-band dual-polarization radar-based hydrometeor classification for Brazilian tropical precipitation systems. *Atmos. Meas. Tech.* **2019**, *12*, 811–837. [CrossRef]
3. Wang, X.; Huang, X.; Ma, S. Observation and Analysis of Two Heavy Rainfall Events Using X-Band Phased Array Weather Radar. *J. Trop. Meteorol.* **2025**, *41*, 553–565. [CrossRef]
4. Chen, H.; Geng, F.; Liu, L.; Yang, H. Study on Precipitation Observation and Retrieval Methods of X-band Phased Array Polarization Weather Radar in Motuo, Xizang. *Plateau Meteorol.* **2024**, *43*, 99–113. [CrossRef]
5. Zhao, Y.; He, B.; Tu, Y. Research on Flood Simulation Based on X-band Radar Quantitative Precipitation Estimation. *J. China Hydrol.* **2026**, *46*, 31–38. [CrossRef]
6. Liu, J.; Yan, C.; Wang, S.; Zhang, P.; Wang, P.; Han, Z. Research on the Application of X-Band Water Conservancy Rain Measurement Radar in the Sanmenxia-Xiaolangdi Section of the Yellow River. *Yellow River* **2025**, *47*, 22–26. [CrossRef]
7. Liu, X.; Wang, F.; Wu, Y.; Xiong, Z.; Wang, S.; Liu, W. Application of X-band Precipitation Radar System to Rainfall Monitoring over Poyang Lake. *Yangtze River* **2024**, *55*, 79–85. [CrossRef]
8. Liu, C.; Liu, Q.; Tian, J.; Liu, Y.; Wang, Y.; Wang, C. Application of X-hand full polarization frequency modulated continuous wave precipitation radar in flash flood forecasting and early warnings. *China Flod Drought Manag.* **2020**, *30*, 48–53. [CrossRef]
9. Zhao, Z.; Tian, F.; Wang, L.; Sun, F.; Liu, W.; Qi, Y. Construction and application of water control precipitation radar: Effectiveness analysis of monitoring flood-causing rainstorms in the Yongding River Basin. *China Water Resour.* **2025**, *12*, 45–51. [CrossRef]
10. Zhang, L.; Li, F.; Feng, W.; Liu, X. Research of Data Quality Analysis and Bias Correction on Mobile X-Band Dual-Polarization Weather Radar. *Meteorol. Mon.* **2021**, *47*, 337–347. [CrossRef]
11. Hubbert, J.C.; Dixon, M.; Ellis, S.M. Weather Radar Ground Clutter. Part II: Real-Time Identification and Filtering. *J. Atmos. Ocean. Technol.* **2009**, *26*, 1181–1197. [CrossRef]
12. Su, T.; Ge, J.; Yang, C. Characteristics and Suppression of Electromagnetic Interference Clutter in CINRAD. *Mod. Radar* **2020**, *42*, 26–31. [CrossRef]
13. Bech, J.; Codina, B.; Lorente, J.; Bebbington, D. The Sensitivity of Single Polarization Weather Radar Beam Blockage Correction to Variability in the Vertical Refractivity Gradient. *J. Atmos. Ocean. Technol.* **2003**, *20*, 845–855. [CrossRef]
14. Berenguer, M.; Sempere-Torres, D.; Corral, C.; Sánchez-Diezma, R. A Fuzzy Logic Technique for Identifying Nonprecipitating Echoes in Radar Scans. *J. Atmos. Ocean. Technol.* **2006**, *23*, 1157–1180. [CrossRef]
15. Wang, Z.; Zhang, P. Relationship Between Attenuation of Microwaves by Polydisperse Small Spheroid Particles and Theirradar Reflectivity Factor. *Acta Meteorol. Sin.* **2000**, *58*, 123–128. [CrossRef]
16. Park, S.; Bringi, V.N.; Chandrasekar, V.; Maki, M.; Iwanami, K. Correction of Radar Reflectivity and Differential Reflectivity for Rain Attenuation atX Band. Part I: Theoretical and Empirical Basis. *J. Atmos. Ocean. Technol.* **2005**, *22*, 1621–1632. [CrossRef]
17. Park, S.-G.; Maki, M.; Iwanami, K.; Bringi, V.N.; Chandrasekar, V. Correction of Radar Reflectivity and Differential Reflectivity for Rain Attenuation at X Band. Part II: Evaluation and Application. *J. Atmos. Ocean. Technol.* **2005**, *22*, 1633–1655. [CrossRef]
18. Zhang, P.; Wang, Z. A Study on Algorithm to Make Attenuation Correction to Radar Observations of Radar Reflectivity Factor(I):Theoretical Analysis. *Plateau Meteorol.* **2001**, *20*, 1–5.
19. Gou, Y.; Chen, H. Correction of Radar Reflectivity From Gap-Filling X-Band Radar Observations. *IEEE Trans. Geosci. Remote Sens.* **2025**, *63*, 5105211. [CrossRef]
20. Li, Q.; Qi, Y.; Zhu, Z.; Yang, Y.; Min, J.; Shi, C.; Zhang, Z.; Li, D.; Wang, N.; Hu, Q. Quantitative precipitation estimation algorithm for C-band radar situated in complex topographical regions. *Acta Meteorol. Sin.* **2021**, *79*, 689–702. [CrossRef]
21. Ramanamahefa, A.V.; Padmanabhan, T.; Lesage, G.; Van Baelen, J. Rain gauges and X-band radar hourly comparison under complex orographic conditions in Reunion Island during the passage of the tropical cyclone Batsirai. *Atmos. Meas. Tech.* **2026**, *19*, 3741–3759. [CrossRef]

22. Luo, L.; Jing, G.; Guo, J.; You, Y. Study on Weather Radar Echo Block Correction Technology of Beijing Meteorological Bureau. *Sci. Technol. Eng.* **2015**, *16*, 12–19.
23. Yu, N.; Gaussiat, N.; Tabary, P. Polarimetric X-band weather radars for quantitative precipitation estimation in mountainous regions. *Q. J. R. Meteorol. Soc.* **2018**, *144*, 2603–2619. [CrossRef]
24. Purnell, D.J.; Kirshbaum, D.J. Synoptic Control over Orographic Precipitation Distributions during the Olympics Mountains Experiment (OLYMPEX). *Mon. Weather Rev.* **2018**, *146*, 1023–1044. [CrossRef]
25. Delrieu, G.; Khanal, A.K.; Yu, N.; Cazenave, F.; Boudevillain, B.; Gaussiat, N. Preliminary investigation of the relationship between differential phase shift and path-integrated attenuation at the X band frequency in an Alpine environment. *Atmos. Meas. Tech.* **2020**, *13*, 3731–3749. [CrossRef]
26. Marshall, J.S.; Palmer, W.M.K. The Distribution of Raindrops with Size. *J. Atmos. Sci.* **1948**, *5*, 165–166. [CrossRef]
27. Delrieu, G.; Khanal, A.K.; Cazenave, F.; Boudevillain, B. Sensitivity analysis of attenuation in convective rainfall at X-band frequency using the mountain reference technique. *Atmos. Meas. Tech.* **2022**, *15*, 3297–3314. [CrossRef]
28. Loulli, E.; Michaelides, S.; Bühl, J.; Loukas, A.; Hadjimitsis, D.G. Correction of path integrated attenuation using data from two X-band ground-based radars and GPM. *Atmos. Res.* **2025**, *321*, 108080. [CrossRef]